HiPERCAM: a quintuple-beam, high-speed optical imager on the 10.4-m Gran Telescopio Canarias

V. S. Dhillon [1,2]★ N. Bezawada,[3] M. Black,[4] S. D. Dixon,[1] T. Gamble,[1] X. Gao,[4] D. M. Henry,[4] P. Kerry,[1] S. P. Littlefair,[1] D. W. Lunney,[4] T. R. Marsh,[5] C. Miller,[4] S. G. Parsons [1] R. P. Ashley,[5] E. Breedt [6] A. Brown [1] M. J. Dyer [1] M. J. Green [5] I. Pelisoli [5] D. I. Sahman,[1] J. Wild [1] D. J. Ives,[3] L. Mehrgan,[3] J. Stegmeier,[3] C. M. Dubbeldam,[7] T. J. Morris,[7] J. Osborn [7] R. W. Wilson [7] J. Casares,[2,8] T. Muñoz-Darias [2,8] E. Pallé,[2,8] P. Rodríguez-Gil,[2,8] T. Shahbaz [2,8] M. A. P. Torres [2,8] A. de Ugarte Postigo,[9] A. Cabrera-Lavers,[10,2] R. L. M. Corradi,[10,2] R. D. Domínguez[10,2] and D. García-Alvarez[10,2]

[1]*Department of Physics and Astronomy, University of Sheffield, Sheffield S3 7RH, UK*
[2]*Instituto de Astrofísica de Canarias, E-38205 La Laguna, Tenerife, Spain*
[3]*European Southern Observatory, D-85748 Garching bei München, Germany*
[4]*UK Astronomy Technology Centre, Royal Observatory Edinburgh, Edinburgh EH9 3HJ, UK*
[5]*Department of Physics, University of Warwick, Coventry CV4 7AL, UK*
[6]*Institute of Astronomy, University of Cambridge, Madingley Road, Cambridge CB3 0HA, UK*
[7]*Department of Physics, University of Durham, Durham DH1 3LE, UK*
[8]*Departamento de Astrofísica, Universidad de La Laguna s/n, E-38206 La Laguna, Tenerife, Spain*
[9]*Instituto de Astrofísica de Andalucía (IAA-CSIC), Glorieta de la Astronomía s/n, E-18008 Granada, Spain*
[10]*GRANTECAN, Cuesta de San José s/n, E-38712 Breña Baja, La Palma, Spain*

ABSTRACT

HiPERCAM is a portable, quintuple-beam optical imager that saw first light on the 10.4-m Gran Telescopio Canarias (GTC) in 2018. The instrument uses re-imaging optics and four dichroic beamsplitters to record $u_s\, g_s\, r_s\, i_s\, z_s$ (320–1060 nm) images simultaneously on its five CCD cameras, each of 3.1-arcmin (diagonal) field of view. The detectors in HiPERCAM are frame-transfer devices cooled thermo-electrically to 183 K, thereby allowing both long-exposure, deep imaging of faint targets, as well as high-speed (over 1000 windowed frames per second) imaging of rapidly varying targets. A comparison-star pick-off system in the telescope focal plane increases the effective field of view to 6.7 arcmin for differential photometry. Combining HiPERCAM with the world's largest optical telescope enables the detection of astronomical sources to $g_s \sim 23$ in 1 s and $g_s \sim 28$ in 1 h. In this paper, we describe the scientific motivation behind HiPERCAM, present its design, report on its measured performance, and outline some planned enhancements.

Key words: instrumentation: detectors – instrumentation: photometers – techniques: photometric.

1 INTRODUCTION

The advent of powerful time-domain survey facilities, such as the Zwicky Transient Facility (ZTF; Graham et al. 2019), the Vera Rubin Observatory (VRO; LSST Science Collaboration et al. 2009), and the Gravitational-wave Optical Transient Observer (GOTO; Dyer et al. 2018), will revolutionize our knowledge of the Universe in the coming decades. Detailed follow-up observations of the most interesting objects discovered by such surveys will be essential if we are to understand the astrophysics of the sources. Although the largest telescopes in the world do provide instrumentation for such follow-up work, one area is poorly catered for – high-speed (seconds to milliseconds) optical cameras.

High time resolution probes allows one to test fundamental physics by probing the most extreme cosmic environments – black holes, neutron stars, and white dwarfs. For example, neutron stars and black holes allow the effects of strong-field general relativity to be studied, and white dwarfs and neutron stars provide us with the opportunity to study exotic states of matter predicted by quantum mechanics (e.g. Antoniadis et al. 2013). White dwarfs, neutron stars and black holes are also a fossil record of stellar evolution, and the evolution of such objects within binaries is responsible for some of the Universe's most exotic phenomena, such as short gamma-ray bursts, millisecond pulsar binaries, Type Ia supernovae, and possibly fast radio bursts (FRBs; e.g. Levin, Beloborodov & Bransgrove 2020).

One way of studying compact objects is through their photometric variability in multiple colours. The dynamical time-scales of white dwarfs, neutron stars and black holes range from seconds to milliseconds, and hence the pulsation and rotation of these objects, and the motion of any material in close proximity to them (e.g.

★ E-mail: vik.dhillon@sheffield.ac.uk

in an accretion disc), tends to occur on these short time-scales. Therefore, the variability of compact objects can only be resolved by observing at high speeds, providing information on their masses, radii, internal structures, and emission mechanisms (e.g. Gandhi et al. 2017; Parsons et al. 2017).

Observing the Universe on time-scales of seconds to milliseconds is also of benefit when studying less massive compact objects, such as brown dwarfs, exoplanets, and Solar system objects. Although the eclipses and transits of exoplanets occur on time-scales of minutes to hours, observing them at high time resolution can significantly improve throughput due to the avoidance of detector readout time, and enables the detection of Earth-mass planets through small variations in transit timing. By observing in multiple colours simultaneously, transit light curves of exoplanets are also sensitive to wavelength-dependent opacity sources in their atmospheres (e.g. Kirk et al. 2016). High time resolution occultation observations of Solar system objects enable their shapes and sizes to be measured, and allow one to detect atmospheres, satellites and ring systems at spatial scales (0.0005 arcsec) only otherwise achievable from dedicated space missions (see Ortiz et al. 2012).

In this paper, we describe a new high-speed camera called HiPERCAM,[1] for High PERformance CAMera, mounted on the world's largest optical telescope – the 10.4-m Gran Telescopio Canarias (GTC) on La Palma. HiPERCAM has been designed to study compact objects of all classes, including white dwarfs, neutron stars, black holes, brown dwarfs, exoplanets, and the minor bodies of the Solar system. However, HiPERCAM is much more than just a high-speed camera – it can equally be used for deep imaging of extended extragalactic targets simultaneously in five optical colours, making it an extremely efficient general-purpose optical imager for the GTC. Brief descriptions of the instrument during the early design and commissioning phases have been provided by Dhillon et al. (2016, 2018) and Bezawada et al. (2018), but no detailed description of the final instrument has appeared in the refereed astronomical literature – a situation rectified by this paper.

2 DESIGN

HiPERCAM was designed to be a significant advance upon its predecessor, ULTRACAM[2] (Dhillon et al. 2007). ULTRACAM saw first light in 2002 and has since been used for nearly 700 nights on the 4.2-m William Herschel Telescope (WHT) on La Palma, the 8.2-m Very Large Telescope (VLT) at Paranal, and the 3.5-m New Technology Telescope (NTT) on La Silla, where it is now permanently mounted. Some of the scientific highlights of ULTRACAM include the discovery of brown-dwarf mass donors in cataclysmic variables (Littlefair et al. 2006), discovery of the first white dwarf pulsar (Marsh et al. 2016), and measurement of the size and albedo of the dwarf planet Makemake (Ortiz et al. 2012).

The HiPERCAM project began in 2014 and saw first light 4 yr later as a visitor instrument on the GTC, on budget (€ 3.5M) and on time. HiPERCAM's performance far exceeds that of UL-TRACAM. HiPERCAM can image simultaneously in five SDSS (Sloan Digital Sky Survey) bands (*ugriz*) rather than the three bands of ULTRACAM (*ugr*, *ugi*, or *ugz*). HiPERCAM can frame at windowed rates of over 1 kHz, rather than the few hundred Hz of ULTRACAM. HiPERCAM uses detectors cooled to 183 K

compared to the 233 K of ULTRACAM, with deep-depletion, anti-etalon CCDs in the red channels (see Section 3.1), resulting in much lower dark current, higher quantum efficiency, and lower fringing than those in ULTRACAM. Hence, although designed for high-speed observations, HiPERCAM is also well suited to science programs that require deep (i.e. long exposure), single-shot spectral-energy distributions, such as light curves of extragalactic transients (e.g. Lyman et al. 2018) and stellar population studies of low-surface-brightness galaxies (e.g. Trujillo & Fliri 2016). HiPERCAM also has twice the field of view of ULTRACAM (when mounted on the same telescope) and a novel comparison-star pick-off system, providing more comparison stars for differential photometry of bright targets, such as the host stars of transiting exoplanets. Each of these design improvements are described in greater detail below.

2.1 Optics

Like ULTRACAM, HiPERCAM was originally designed to be a visitor instrument, moving between 4 and 10 m class telescopes in both hemispheres to maximize its scientific potential. Hence, the baseline optical design for HiPERCAM was optimized to provide good imaging performance on the WHT, NTT, and GTC.

2.1.1 Requirements

The main requirements of the HiPERCAM optics were as follows:

(i) To provide simultaneous imaging in five optical bands covering the SDSS *ugriz* filter bandpasses from 320 to 1000 nm (Fukugita et al. 1996).

(ii) To give a plate scale of 0.3 arcsec pixel^{-1} on the WHT. Using an e2v 231-42 CCD with 2048 × 1024 imaging pixels, each of 15 μm in size (see Section 3.1), this plate scale would provide a field of view of 10.24 × 5.12 arcmin^2 on the WHT.

(iii) The optics should not degrade the point spread function (PSF) by more than 10 per cent, measured over 80 per cent (radius) of the field of view in median WHT seeing conditions (see Wilson et al. 1999) of 0.68/0.64/0.61/0.58/0.56 arcsec in *ugriz*. Hence, in seeing of 0.68 arcsec in the *u* band, for example, the stellar PSFs should have FWHM (full width at half-maximum) of <0.75 arcsec out to a field radius of 4.5 arcmin.

(iv) The plate scale should be constant across this wavelength range to within 0.0005 arcsec pixel^{-1}, thereby ensuring that stars have the same CCD pixel positions in each band, to within ± 1 pixel (assuming perfect alignment of the CCDs relative to each other).

(v) The optical design should be optimized so that the image quality of HiPERCAM when used on the NTT and GTC should be equivalent to that on the WHT. Using the CCD specified in (ii), the optics would provide a plate scale of 0.357 and 0.081 arcsec pixel^{-1}, and a field of view of 12.18 × 6.09 and 2.76 × 1.38 arcmin^2, on the NTT and GTC, respectively.

2.1.2 Layout

A ray trace through the HiPERCAM optics is shown in Fig. 1(a). Light from the telescope focal plane is first collimated by a four-element collimator. It then passes through four dichroic beamsplitters that split the light into five wavebands. Each of the five collimated beams is then focused by a re-imaging camera on to a detector. The re-imaging cameras are of a double-Gauss type design with two singlet lenses and two cemented doublet lenses arranged in a roughly symmetrical layout around the re-imaged pupil. The

---
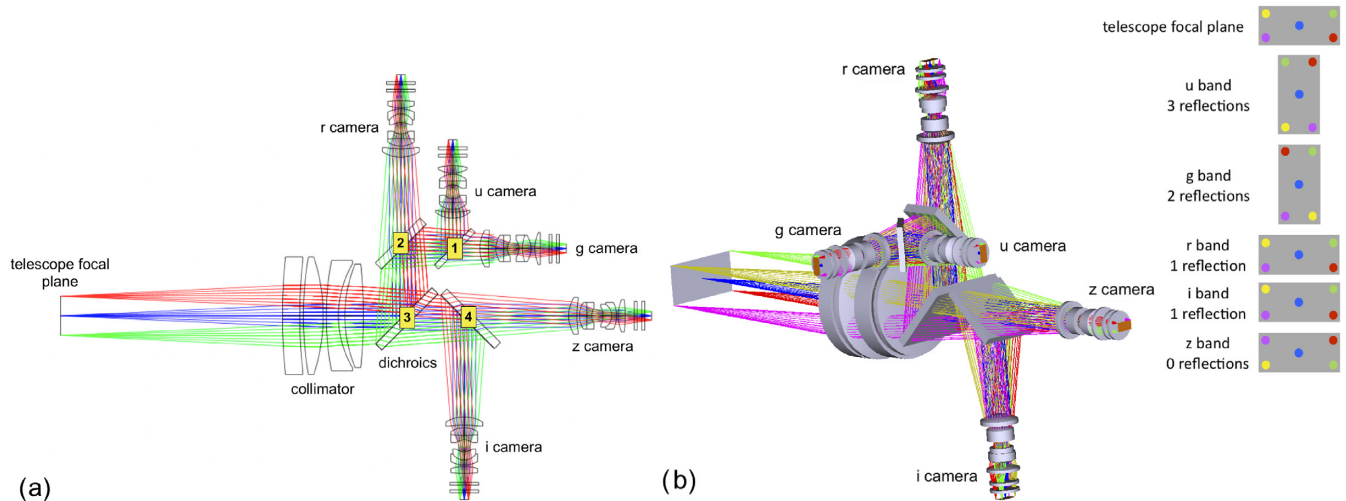
Figure 1. Panel (a): ray trace through the HiPERCAM optics. The red, green, and blue lines represent ray bundles emanating from three spatially separated point sources in the telescope focal plane. The diagram is to scale – for reference, the diameter of the largest lens in the collimator is 219 mm. The yellow boxes show the dichroic numbers, which are in ascending order of the cut-point wavelength, as shown in Fig. 2. Panel (b): Three-dimensional view of the HiPERCAM optics, showing the dichroic rotations used to package the instrument more efficiently. The orientation of each detector with respect to the telescope focal plane is shown on the far right, with the coloured spots corresponding to the bundles of rays of the same colour shown in the three-dimensional view.

light then travels through a bandpass filter and a cryostat window before striking the detector.

The layout in Fig. 1(a) shows all five cameras in the same plane; this is for clarity only, and in reality, a more compact packaging of the dichroics and associated re-imaging cameras has been achieved by rotating them around the optical axis of the system, as shown in Fig. 1(b). As a result of the differing number of dichroic reflections experienced by the beams, the images falling on the detectors are flipped with respect to each other (see the coloured spots at the far right in Fig. 1b). This is corrected in the data acquisition software (see Section 3.2) to ensure that the output images have the same orientation and left-right/top-bottom flip.

The HiPERCAM collimator and re-imaging cameras together operate as a focal reducer, demagnifying the image in the telescope focal plane by a factor of 0.225, given by the ratio of the re-imaging camera focal length (98.6 mm) to the collimator focal length (437.3 mm). A summary of the main optical parameters of HiPERCAM on the three telescopes for which the optical design was optimized is given in Table 1. Note that an optical design does exist for a separate GTC collimator that, with no change to any of the other HiPERCAM optics, would increase the detector pixel scale and field of view to 0.113 arcsec/pixel and 3.84×1.68 arcmin^2, respectively. However, given its high cost, the excellent image quality obtained on the GTC with the existing collimator, and the effective increase in the field of view of HiPERCAM on the GTC afforded by COMPO (see Section 5.1), this second collimator has not been built.

The four-lens collimator is the first optical component and hence must have high transmission across the required 320–1000 nm wavelength range. The glasses chosen were therefore N-BAK2, CaF$_2$, and LLF1, with the largest lens of diameter 219 mm. The six-element re-imaging cameras for the three longer wavebands (*riz*) share a common optical design, but the *ug* camera designs are unique in order to maximize throughput and image quality. The first element in each re-imaging camera was manufactured last, to re-optimized radii of curvature and thicknesses based on the as-built properties of the other five lenses. This compensated for differences in glass dispersion and tolerance build-up, thereby ensuring that all bands have the same effective pixel scale and optimum image quality.

The lens–lens axial spacings were also re-optimized during this process. All lenses were antireflection coated, with the collimator lenses receiving a broad-band coating with average reflectivity of < 2 per cent, and the re-imaging lenses receiving a narrow-band coating with average reflectivity < 0.5 per cent. The HiPERCAM lenses were manufactured by the Rocky Mountain Instrument Company, Colorado, who also performed the antireflection coating and mounted the lenses in aluminium barrels (see Section 3).

The four dichroic beamsplitters are made of fused silica, with the largest of dimension 140×150 mm. The front faces of the dichroics are coated with long-wave pass coatings that reflect incident light with wavelengths shorter than the cut-points and transmit longer wavelengths. The dichroic cut points are shown in Fig. 2 and were selected to maximize the throughput in the two adjacent filter bandpasses. This calculation was performed after the filters had been manufactured and hence their as-built bandpasses were known. The difference between the wavelengths at which 90 and 10 per cent transmission occurs is < 15.5 nm, and the reflectance/transmission of wavelengths shorter/longer than the cut points is > 99.5 and > 98 per cent, respectively. To maximize throughput and minimize ghosting, the rear of each dichroic is coated with a narrow-band antireflection coating of average reflectivity < 0.5 per cent. Detailed modelling of the ghosting in the HiPERCAM optics showed that the brightest ghosts are $\sim 10^7$ times fainter than the primary image, which is insignificant given that the dynamic range of the detector is of the order of 10^4.

The bandpasses of HiPERCAM's five arms are defined by a set of so-called 'Super' SDSS filters (Fig. 2). These filters, which we refer to as $u_s g_s r_s i_s z_s$, were specifically designed for HiPERCAM, with cut-on/off wavelengths that match the original SDSS *ugriz* filters (Fukugita et al. 1996) but which use multilayer coatings rather than coloured glasses to define the bandpasses and increase throughput. The $u_s g_s r_s i_s z_s$ filters provide a throughput improvement of 41/9/6/9/5 per cent compared to *ugriz* filters, respectively. Since the whole optical spectrum is being covered in one shot by HiPERCAM, we decided not to install filter wheels in front of each CCD. Instead, each filter is mounted in a cartridge that can be easily changed by hand, if required. The HiPERCAM filters are of identical dimensions

Table 1. Summary of the main optical parameters of HiPERCAM on the three telescopes for which the optical design was optimized.

	WHT	NTT	GTC
Telescope design	Cassegrain	Ritchey–Chrétien	Ritchey–Chrétien
Entrance pupil diameter (mm)	4179.0	3500.0	11 053.4[a]
Effective focal length (mm)	45 737.5	38 501.7	169 897.7
Telescope f-ratio	10.95	11.00	15.415
Telescope focal-plane scale (arcsec mm^{-1})	4.510	5.357	1.214
Detector plate scale (arcsec mm^{-1})	20.0	23.759	5.382
Detector pixel scale (arcsec pixel^{-1})	0.300	0.356	0.081
Detector field of view (arcmin)	10.24×5.12	12.16×6.08	2.76×1.38
Internal pupil diameter[b] (mm)	21.7	21.4	15.5
f-ratio at detector	2.468	2.480	3.465

[a]This is the distance across the segmented, hexagonal primary mirror. The diameter of a circular mirror with the same collecting area as the GTC primary would be 10.4 m.

[b]This is the diameter of the intermediate pupil lying within the re-imaging cameras that is conjugate with the entrance aperture of the telescope. The entrance aperture of the GTC lies at the secondary mirror, whereas on the WHT and NTT it is the primary mirror.
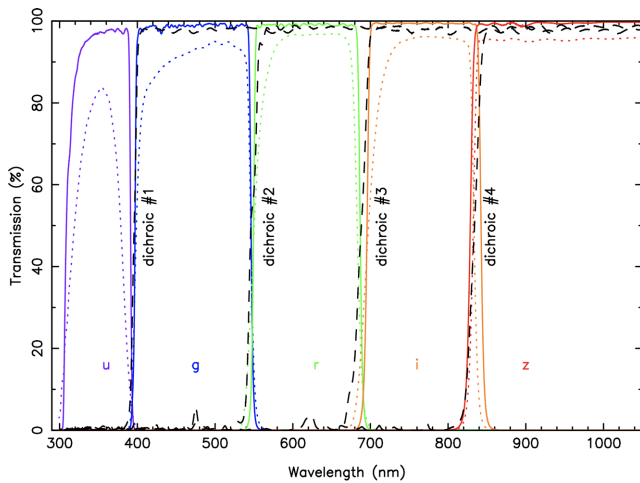
Figure 2. Transmission profiles of the as-built HiPERCAM dichroic beam-splitters (dashed lines), the HiPERCAM 'original' SDSS filters (dotted lines), and the HiPERCAM 'Super' SDSS filters (solid lines). One of the main advantages of HiPERCAM over its predecessor, ULTRACAM, is that one no longer has to choose which of *riz* to select for the red arm filter, as all three are simultaneously available.

$(50 \times 50 \text{ mm})$ and optical thicknesses to the ULTRACAM filters, which means that the extensive set of ULTRACAM narrow-band absorption-line, emission-line, and continuum filters[3] can be used in HiPERCAM.

The final element in the optical path of each HiPERCAM arm is a fused-silica window, which allows light on to the CCD whilst forming a vacuum seal with the detector head (see Section 3.1). The windows have broad-band antireflection coatings with average reflectivity of < 1 per cent. The HiPERCAM dichroics, filters, and windows were all manufactured by Asahi Spectra Company, Tokyo. The HiPERCAM optics are far superior in terms of throughput and image quality compared to ULTRACAM, having benefitted from a ten-fold increase in the optics budget and nearly two decades of improvement in optical manufacturing and coating techniques.

[3]http://www.vikdhillon.staff.shef.ac.uk/ultracam/filters/filters.html.

3 MECHANICAL DESIGN

The mechanical structure of HiPERCAM was designed to meet the following requirements:

(i) Provide a rigid platform on which to mount the optics and CCD heads, with relative flexure between the CCD heads of less than ~1 pixel (15 μm) at any instrument orientation, so that stars do not drift out of small windows defined on the five CCDs.

(ii) Provide a mounting for the CCD controller, which must lie within a cable length of ~1.5 m of the CCD heads to minimize pickup noise and clock-signal degradation.

(iii) Allow access to the CCD heads for maintenance, alignment, and filter changes.

(iv) Minimize thermal expansion for focus stability.

(v) Provide electrical and thermal isolation from the telescope to reduce pickup noise via ground loops and minimize the load on the water cooling system.

(vi) Provide a light-tight and dust-proof environment for the optics.

(vii) Have a total weight of < 1000 kg, set by the mass limit of the GTC rotator, and size < 1.3m × 1.0 m × 1.0 m, set by the intersection of the GTC instrument space envelope at the Folded Cassegrain focus and the maximum dimensions of a single item that can be air freighted to La Palma.

To meet the above requirements, the HiPERCAM opto-mechanical chassis is composed of three aluminium plates connected by carbon fibre struts. This triple-octopod design is shown in Fig. 3 and provides an open, stiff, compact (1.25-m long) and light-weight (288 kg) structure that is relatively insensitive to temperature fluctuations. These characteristics also make it straightforward to transport, maintain, and mount/dismount HiPERCAM at the telescope. The collimator, dichroics, re-imaging lenses, filters, and CCD heads are all housed in/on an aluminium hull that forms a sealed system to dust and light. The hull is attached to the central aluminium plate, the CCD controller is mounted in a cradle hanging off the bottom plate, and the top plate connects the instrument to the telescope, as shown in Fig. 3. A steel interface collar attaches HiPERCAM to the rotator and places the instrument at the correct back-focal distance. A layer of G10/40 epoxy glass laminate is located between the top plate of HiPERCAM and the collar to
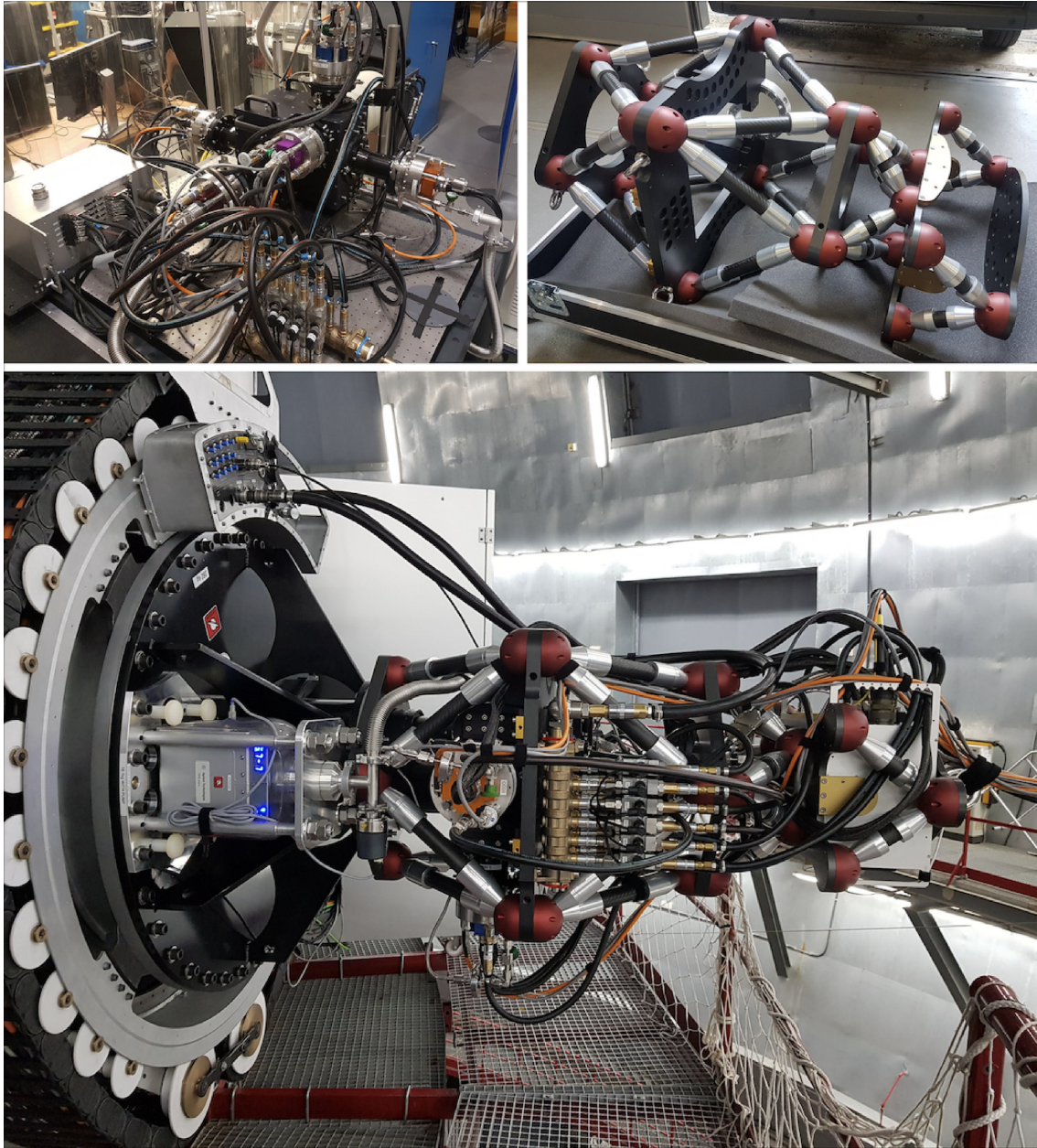
Figure 3. Top left-hand panel: the HiPERCAM hull during alignment at the UK Astronomy Technology Centre (UKATC). The hull is the black box at the centre of the image. The five re-imaging cameras and CCD heads can be seen attached to the hull. The rears of the CCD heads are anodized according to the filter colour (u_s = violet, g_s = blue, r_s = orange, i_s = red, z_s = dark red) for ease of identification. The aluminium box at the lower left is the CCD controller. Top right-hand panel: the HiPERCAM opto-mechanical chassis during integration at the UKATC. From the left- to right-hand side, the first three vertical black plates are the top plate (which attaches to the telescope), the middle plate (to which the hull is attached), and the bottom plate (to which the cradle holding the CCD controller is attached). For scale, the total length of the opto-mechanical chassis is 1.25 m. Bottom panel: HiPERCAM on the Folded Cassegrain focus of the GTC. From the left- to right-hand side, the rotator (surrounded by its cable wrap), the black HiPERCAM interface collar (on which is mounted the vacuum pump with blue LEDs in the image), and HiPERCAM can be seen.

provide electrical and thermal isolation from the telescope. The mounting collar houses a motorized focal-plane mask. This is an aluminium blade that can be inserted in the telescope focal plane to block light from bright stars falling on the active area of the sensor above the CCD windows, which would otherwise cause vertical streaks in the images. This mask also prevents photons from stars and the sky from contaminating the windows in drift mode (see Section 3.4).

3.1 Detectors

HiPERCAM employs five custom-designed CCD231-42 detectors from Teledyne e2v. The CCDs are split frame-transfer devices with 15 μm pixels and four outputs, with one output located at each corner. The devices have a format of 2048 × 2080 pixels, where the upper 2048 × 520 and lower 2048 × 520 pixels are coated with reflective aluminium masks and used as frame-transfer storage areas, providing a central image area of 2048 × 1024 pixels. Each CCD
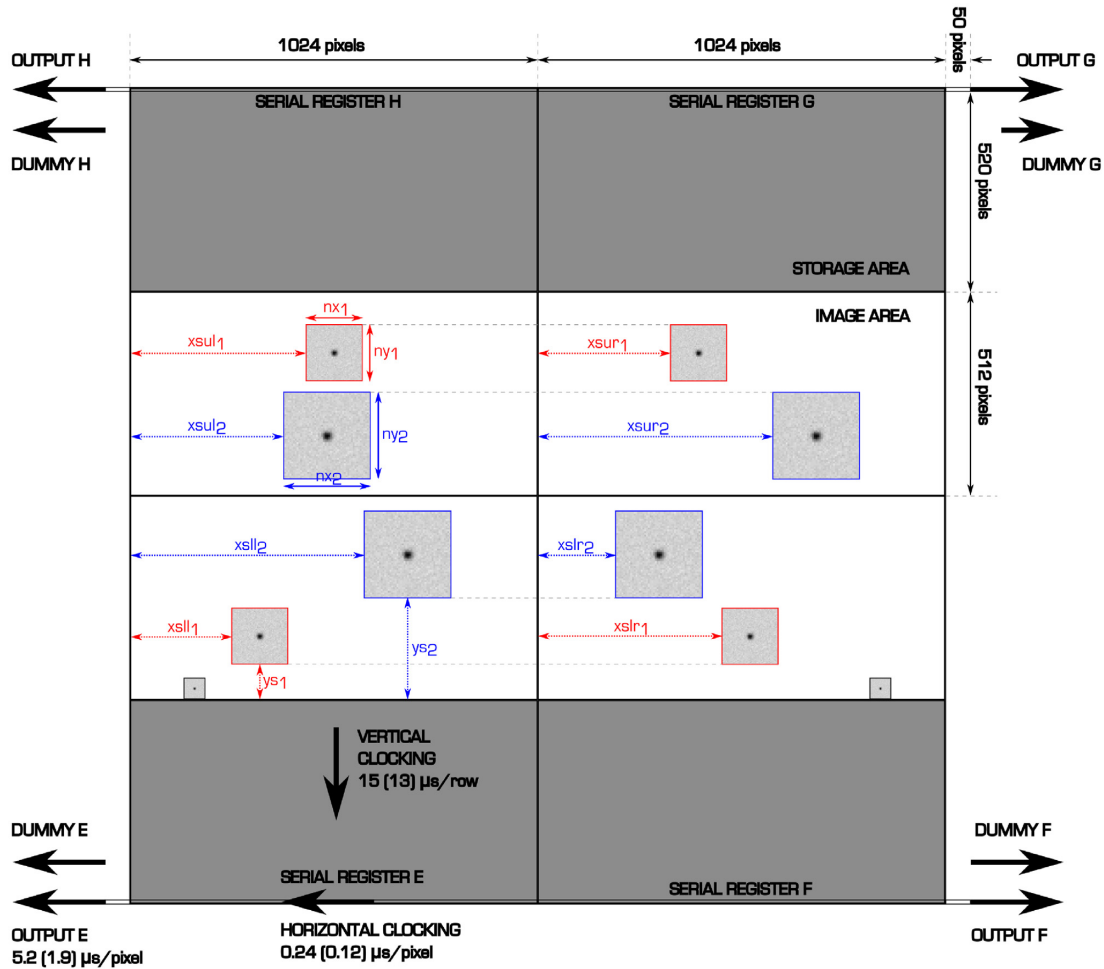
Figure 4. A schematic of the CCD231-42 detector used in HiPERCAM. The CCD has a split frame-transfer architecture with four outputs, labelled E, F, G, and H by e2v, and four dummy outputs for common-mode signal rejection. The image area is shown in white and the storage area in grey. The lower left-hand quadrant is read by output E, the lower right-hand quadrant by F, the upper right-hand quadrant by G, and the upper left-hand quadrant by H. There are four 1024-pixel serial registers, two at the top and two at the bottom of the detector, which can be clocked independently and which have an additional 50 pre-scan pixels for bias-level determination. The storage area is 8 pixels larger in the vertical direction than the image area, and these overscan pixels can also be used to determine the bias level. The pixel and clocking rates indicated in the diagram are for the slow settings – values for the fast settings are given in brackets. The detector can be read out in three different modes: (1) full-frame mode, where the entire white region is read out; (2) windowed mode, where either the four red windows (one 'quad') are read out, or the four red *and* the four blue windows are read out (two quads); and (3) drift mode, where the two small black windows on the border between the lower image and storage areas are read out.

output therefore processes a quadrant of 1024×512 pixels, as shown in Fig. 4.

The CCDs used in HiPERCAM are back-illuminated and thinned to maximize quantum efficiency (QE) – the QE curves are shown in Fig. 5. All of the CCDs are antireflection (AR) coated – the u_s-band CCD with the enhanced (or 'Astro') broad-band coating, and the $g_s r_s i_s z_s$ CCDs with the Astro Multi-2 coating. The $u_s g_s r_s$ CCDs are manufactured from standard silicon and, to maximize red QE, the $i_s z_s$ CCDs are manufactured from deep-depletion silicon. The $i_s z_s$ CCDs have also undergone e2v's fringe suppression (anti-etaloning) process, where irregularities in the surface of the CCD are introduced to break the interference condition. This reduces the i_s-band fringing to essentially zero and the z_s-band fringing to approximately the same level as the ~ 1 per cent flat-field noise (see Tulloch 1995). The HiPERCAM CCDs are of the highest cosmetic quality available (grade 1) and have a full-well capacity of $\sim 115\,000\,e^-$. The CCDs are operated with a system gain of $1.2\,e^-/\mathrm{ADU}$ and 16-bit analogue-to-digital converters (ADCs) in the CCD controller (see Section 3.2),
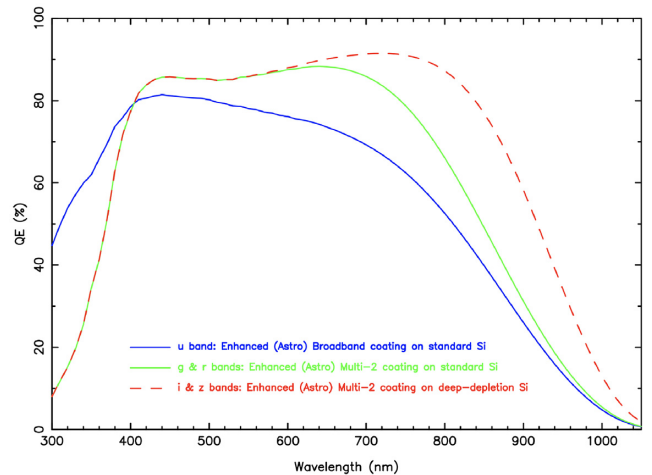
Figure 5. Quantum efficiency curves of the HiPERCAM CCDs at 173 K.
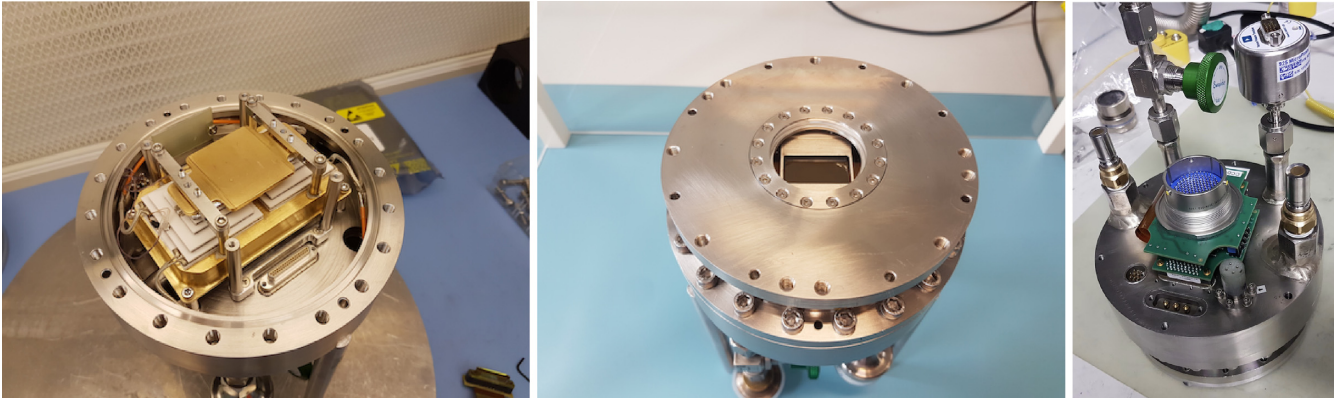
Figure 6. Left-hand panel: a view of the interior of one of the HiPERCAM CCD heads. The gold-plated cold plate on which the CCD is mounted sits on top of two, white five-stage TECs. The two TECs sit side-by-side on a gold-plated heatsink through which the coolant flows. Centre panel: front view of the head, showing the CCD through the window. The weight of the head is approximately 7 kg and its diameter is 160 mm. Right-hand panel: rear view of the head, showing the green pre-amplifier board with blue 128-pin connector, the green vacuum valve, the vacuum gauge, the quick-release connectors for the coolant inlet/outlet, and the connector sockets for the temperature sensors, TEC power, and getter. In this photograph, the colour-anodized aluminium box that provides electromagnetic-interference shielding of the pre-amplifier board (as shown in Fig. 3) has been removed.

thereby adequately sampling the read noise to minimize quantization noise, and ensuring a reasonable match between digital saturation and device saturation.

To minimize read noise and maximize readout speed, the CCDs used in HiPERCAM are equipped with: low noise amplifiers of $3.2\,e^-$ rms at 200-kHz pixel rates (as measured by e2v; see Section 4.3 for readout-noise measurements at the telescope); dummy outputs to eliminate pickup noise; fast serial (horizontal) and vertical (parallel) clocking – see Fig. 4 for rates – whilst retaining CTE (charge-transfer efficiency) of > 99.9995 per cent; independent clocking of the serial register in each quadrant to provide efficient windowing modes (see Section 3.4); two-phase image and storage clocks to minimize the frame-transfer time.

HiPERCAM uses non inverted-mode (NIMO) instead of advanced inverted-mode (AIMO) CCDs. There are four reasons for this. First, it is possible to clock NIMO devices more quickly. Secondly, NIMO devices have greater well depths. Thirdly, although both NIMO and AIMO CCDs can have the same dark current specifications at their optimum operating temperatures, our experience with ULTRASPEC (NIMO; Dhillon et al. 2014) and ULTRACAM (AIMO; Dhillon et al. 2007) is that the dark current in NIMO devices is evenly distributed across the CCD whereas the dark current in AIMO CCDs is in the form of hot pixels that do not subtract well using dark frames, making exposures $\gtrsim 30\,s$ undesirable. Fourthly, we chose to use NIMO devices in HiPERCAM because the red CCDs are made of deep-depletion silicon to maximize QE and this is not compatible with inverted-mode operation.

One consequence of selecting NIMO devices for HiPERCAM is that the CCDs require cooling to below 187 K to reduce the dark current to less than $360\,e^-\,\mathrm{pixel}^{-1}\,\mathrm{h}^{-1}$, corresponding to 10 per cent of the faintest sky level recorded by HiPERCAM (given by u_s-band observations in dark time on the GTC). Therefore, cooling to below 187 K ensures that dark current is always a negligible noise source in HiPERCAM. We considered a number of cooling options to meet this temperature requirement. Liquid nitrogen was rejected as being impractical – five liquid-nitrogen cryostats would make HiPERCAM heavy, large, and time-consuming to fill each night, and continuous flow or automatic filling systems are not viable given that HiPERCAM was designed as a visitor instrument with no requirement for dedicated infrastructure at the telescope. We also

rejected closed-cycle Joule-Thomson coolers, such as the CryoTiger, as it would be difficult to pass 10 stainless-steel braided gas lines through the cable wrap and accommodate the five compressors at the telescope. Stirling coolers were given serious consideration, but we were concerned about the impact of their vibrations on the image quality at the telescope. Although the vibrations can be reduced, e.g. through the use of complex, bulky antivibration mounts (Raskin et al. 2013), even with such precautions in place it would have been difficult to persuade the potential host telescopes to accept HiPERCAM as a visitor instrument due to the residual vibrations. Finally, after extensive prototyping and testing to verify that they could achieve the required CCD temperature, we selected thermo-electric (Peltier) coolers (TECs), as they are the cheapest, simplest, lightest and most compact of all of the cooling options.

Our cooling solution, implemented by Universal Cryogenics, Tucson, uses two side-by-side Marlow NL5010 five-stage TECs, as shown in Fig. 6. The detector heads are manufactured from stainless steel and use all-metal seals rather than rubber o-rings in order to minimize vacuum leaks. Wherever possible, we avoided the use of materials that could outgas inside the detectors heads. So, for example, the pre-amplifier boards were mounted outside the heads (see Bezawada et al. 2018 for details); corrugated indium foil was used for the thermal connections between the cold plate, TECs, and heatsink; we installed a non-evaporable porous getter in each head that acts as an internal vacuum pump and can be periodically re-activated by heating to 500°C using an external power supply. Outgassing was further minimized by cleaning the components ultrasonically prior to assembly, and baking the assembled head whilst vacuum pumping. Even with these precautions, the vacuum hold time of the HiPERCAM CCD heads at pressures below the $\sim 10^{-3}$ mbar range is only of order weeks, due primarily to the lack of a sufficiently cold, large-area interior surface to give effective cryopumping, and residual outgassing in the small interior volume (~ 0.5 litre) of the heads. The low-volume heads do, however, have the advantage of requiring only a few minutes of pumping to bring them back down to their operating pressure using a five-way vacuum manifold circuit permanently installed on HiPERCAM.

A copper heatsink connected to the 278 K water-glycol cooling circuit at the GTC is used to extract the heat generated by the TECs in each CCD head. The heatsinks in the five CCD heads are connected
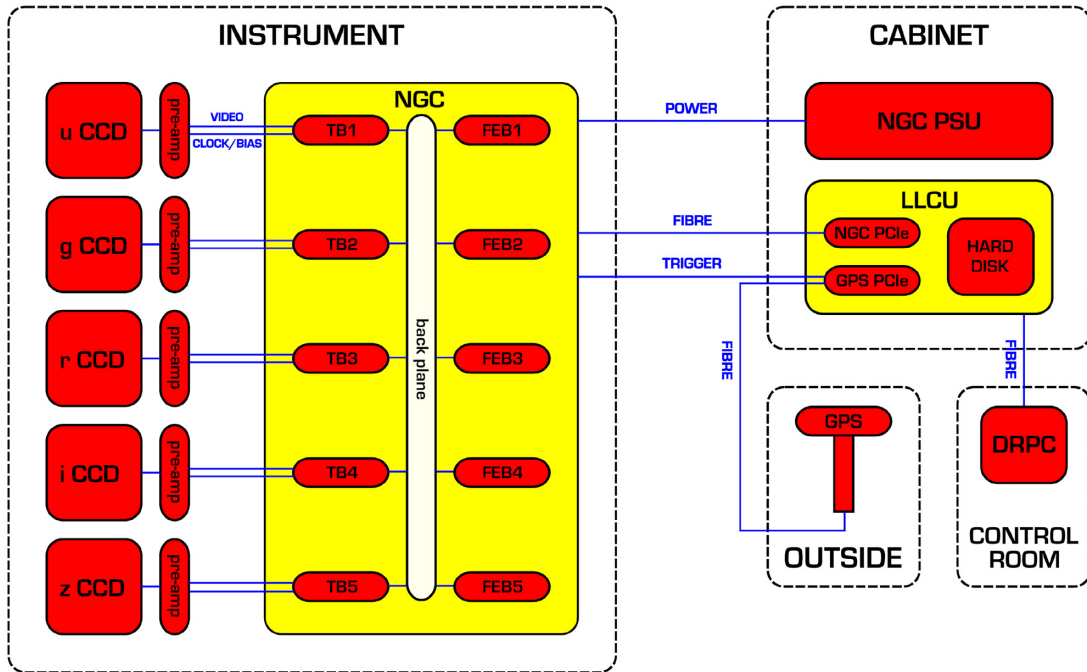
Figure 7. A block diagram showing the hardware of the HiPERCAM data acquisition system – see Section 3.2.1 for details.

in parallel using two six-way manifolds (with the sixth channel for cooling the CCD controller), thereby ensuring that cooling fluid of the same temperature enters each head. Each of the six cooling channels is equipped with an optical flow sensor made by Titan Enterprises, all of which are connected to a single Honeywell Minitrend GR Data Recorder mounted in the electronics cabinet. The data recorder provides a display of the flow rate in each CCD head and, to protect the CCDs from overheating, it also has relays to turn-off power to the TEC power supplies if the flow rate in any head drops below a user-defined limit. The TEC power supplies (made by Meerstetter, model LTR-1200) have a high-temperature automatic cut-off facility that provides an emergency backup to the flow sensors: If the temperature of the heatsink in a CCD head rises above a user-defined value due to a coolant failure, the power to the TEC is turned off. The TEC power supplies are able to maintain the HiPERCAM CCD temperatures at their 183-K set points to within $0\,\overset{\circ}{.}1$C. At this temperature, the dark current is only $\sim 20\,\mathrm{e^-\,pixel^{-1}\,h^{-1}}$.

To prevent condensation on the CCD windows in high humidity conditions, HiPERCAM employs a five-way manifold that enables dry, clean air from the telescope supply to be blown across the outer faces of the windows at approximately 1 litre min^{-1}. Each CCD head also contains an internal LED that can be turned on and off for a user-specified duration to provide a convenient and controllable light source for testing the detectors.

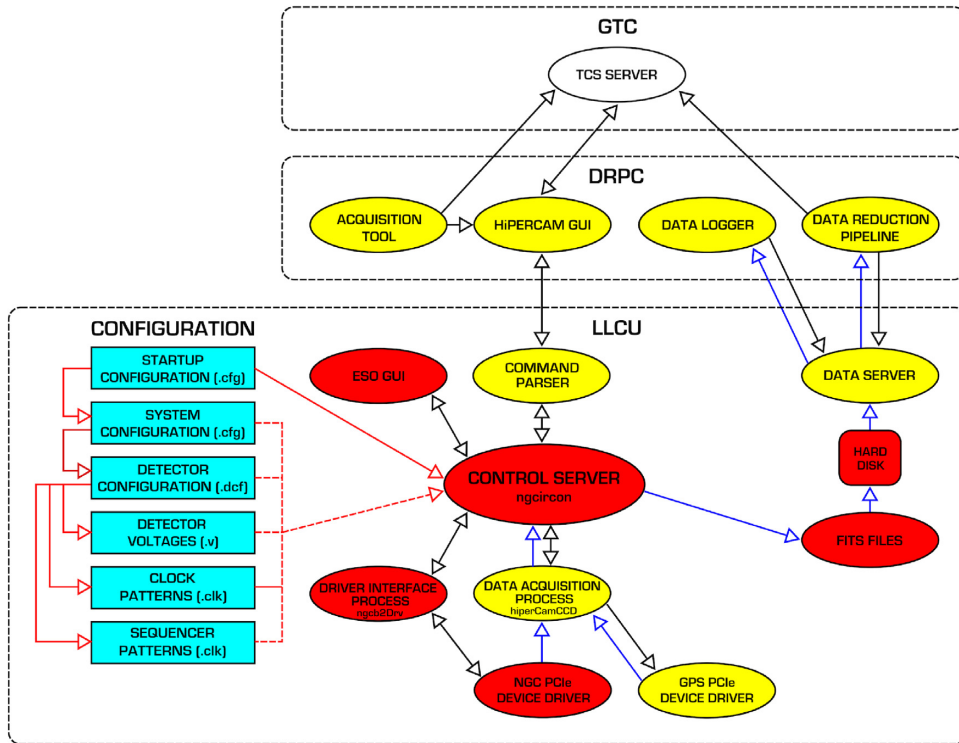### 3.2 Data acquisition system

The HiPERCAM data acquisition system was designed to be detector limited, so that the throughput of data between the CCD outputs and the hard disc (HD) on which it is stored is always greater than the rate at which the data can be clocked off the CCDs. This means that HiPERCAM never has to operate in bursts, periodically pausing so that the data archiving can catch up; instead, HiPERCAM can operate continuously all night, even at its maximum data rate.

3.2.1 Hardware

A block diagram of the HiPERCAM data acquisition hardware is shown in Fig. 7. The architecture is similar to that developed for ULTRACAM (Dhillon et al. 2007), but uses much faster and more modern hardware. At the centre of the system is a European Southern Observatory (ESO) New General detector Controller (NGC; Baade et al. 2009). The NGC used in HiPERCAM is composed of a five-slot housing, with five transition boards (TB) and five front-end basic (FEB) Boards, connected via a back-plane. Each TB handles all of the external connections to its corresponding FEB, and is connected to a CCD via a pre-amplifier board mounted on the back of the CCD head. The pre-amplifier board contains AC-coupled differential pre-amplifier circuits and passive filters, and provides overvoltage and electrostatic discharge protection on the input bias lines (Bezawada et al. 2018). The NGC and pre-amplifier board are connected by a single cable that carries both the CCD video signal to the four differential video processing chains on the associated FEB and the clocks/biases from the clock/bias-driver on the FEB. To minimize the length of the cables ($\sim$1.5 m) running to each CCD head, the NGC is located on the instrument (see Fig. 3). In order to maximize the readout speed, the HiPERCAM NGC has been configured electronically to use the analogue clamp sample (ACS) method, which takes only one sample of the voltage at the CCD output per pixel readout cycle. The NGC can also be configured to use slower dual-slope integration (DSI), which takes two samples per pixel, but we found this did not significantly reduce the read noise (see Section 4.3).

The NGC is powered by a separate power supply unit (PSU), located in an electronics cabinet mounted on the telescope approximately 3 m from HiPERCAM. The cabinet also contains a linux PC known as the LLCU (Linux local control unit). The LLCU was provided by ESO to control the NGC, and contains the NGC Peripheral Computer Interconnect Express (PCIe) card. The NGC PCIe card and NGC are connected by duplex fibre, over which one

Figure 8. Software architecture and configuration of the HiPERCAM data acquisition system. Black arrows show the flow of commands/replies, blue arrows show the flow of CCD data. Red ellipses indicate tasks supplied by ESO as part of the standard NGCIRSW software distribution, yellow ellipses indicate tasks that were modified/written specifically for HiPERCAM, and the white ellipse indicates that the task was provided by the GTC. NGC configuration is shown on the left in the blue boxes: Solid red arrows indicate 'specifies', and dashed red arrows indicate 'reads'.

can receive CCD data and control the NGC. The LLCU also contains a large-capacity HD on which the raw CCD data are written.

The LLCU contains a GPS (Global Positioning System) PCIe card made by Spectracom (model TSync-PCIe-012) that accepts two inputs. The first is a trigger generated by the NGC when an exposure starts, causing the GPS card to write a timestamp to its FIFO (First In, First Out) buffer, which is subsequently written to the corresponding CCD frame header. The second input is a GPS signal from an antenna located outside the dome. The antenna and GPS card are connected by a long (150 m) optical fibre that electrically isolates the telescope from lightning strikes.

The LLCU is connected via fibre ethernet to a second linux PC located in the telescope control room (see Fig. 7), referred to as the Data Reduction PC (DRPC). The DRPC runs the GUI (graphical user interface) to control the instrument, the data reduction pipeline, the target acquisition tool and the data logger, amongst other things.

3.2.2 Software

The NGC is controlled using ESO's NGC Infrared Detector Control Software (NGCIRSW), to which HiPERCAM-specific components have been added, as shown in Fig. 8. For clarity, the first time each of the tasks shown in Fig. 8 is referred to in the text below, it is written in italics.

Communication with the NGC is handled by the *Control Server*, which runs on the LLCU and interacts with the *NGC PCIe Device Driver* via a *Driver Interface Process*. The control server can also be set up to run in simulation mode for development and testing when

no NGC is connected. The *Data Acquisition Process* (or acquisition task) is HiPERCAM specific and also runs on the LLCU. This task begins when the 'START' exposure command is executed, and receives data from the CCDs via the NGC-PCIe card. On completion of an exposure, the acquisition task reads the timestamp from the *GPS PCIe Device Driver*, adds the timestamp to the frame, and passes the data and headers to the *FITS Files* task (via the control server) for writing to the HD. The GPS timestamp is synchronized with the start of the exposure using an external trigger from the NGC. The acquisition task runs continuously until either the required number of CCD exposures have been taken or a 'STOP' exposure command has been issued. The acquisition process can also perform any data pre-processing prior to writing the frame, such as averaging multiple pixel reads for noise reduction (see Section 4.3).

The NGCIRSW suite offers an *ESO GUI* (or 'engineering' GUI), which is useful for testing and development purposes, but for science use has been replaced by the *HiPERCAM GUI* to control the NGC whilst observing. The HiPERCAM GUI is written in PYTHON/TKINTER and runs on the DRPC in the control room. It communicates with the NGC on the telescope using HTTP (Hypertext Transfer Protocol) over TCP/IP (Transmission Control Protocol/Internet Protocol) on a dedicated fibre-ethernet link. The interface between the HiPERCAM GUI and the NGC is the *Command Parser*, which is a PYTHON-based HTTP server running on the LLCU with a RESTful (Representational State Transfer) interface. The command parser translates the HTTP commands issued by the HiPERCAM GUI to low-level NGCIRSW commands to be executed by the NGC, e.g. to start/stop an exposure, change the CCD readout mode, or request information on the current exposure.

The NGC configuration is set using short FITS (Flexible Image Transport System) format files, which are editable by hand if required. There are three types of configuration file – startup, system, and detector configuration, as shown in Fig. 8. The startup configuration file defines the command-list of the control server. The system configuration defines the NGC hardware architecture, such as the number and addresses of the boards in the controller and LLCU. The detector configuration describes which clock patterns, voltages, and sequencer programs to load for the setup requested by the user on the HiPERCAM GUI. The detector voltages are defined in a voltage configuration file, in short FITS format. The clock patterns are described in blocks, with each block defining a sequence of clock states. Clock pattern blocks can be defined in either hand-editable or binary format, the latter output by the ESO graphical editing tool *BlueWave*. The sequencer program defines the order of execution of the defined clock pattern blocks and is written in TCL/TK.

To prepare for observing with HiPERCAM ('Phase II'), astronomers use the *Acquisition Tool* [4] to generate finding charts, specify the telescope pointing and instrument setup, and provide cadence and signal-to-noise ratio estimates. The required telescope pointings and instrument setups are written to JSON (JavaScript Object Notation) files, which are also editable by hand if required. Copies of these files are sent to the GTC Telescope Control System (TCS), to point the telescope at the required fields, and to the HiPERCAM GUI, to set the CCDs up for the required observations.

The HiPERCAM GUI communicates with the telescope via the *TCS Server*. This link provides information on the telescope pointing and focus that can then be written to the FITS headers of the CCD data files. The link also provides a way of tweaking the Right Ascension, Declination, rotator angle, and focus of the telescope, which is useful when acquiring targets and dithering. For the latter, astronomers set up their required patterns using the acquisition tool. The HiPERCAM GUI then executes the dithering pattern, synchronizing the NGC readout so that no exposures are taken whilst the telescope is moving/settling.

3.3 Pipeline data reduction system

HiPERCAM can generate up to 17 MB per second of data, or up to 600 GB per night. To cope with this relatively high data rate, HiPERCAM has a dedicated *Data Reduction Pipeline*,[5] as shown in Fig. 9. The pipeline runs on the DRPC and is written in PYTHON. A PYTHON TCP/IP WebSocket *Data Server* running on the LLCU allows the data on the HD to be accessed by the pipeline over a dedicated fibre-ethernet link (see Figs 7 and 8). The HiPERCAM *Data Logger* accesses the same server to provide observers with a real-time log of the data obtained.

When observing, the HiPERCAM pipeline provides a quick-look data reduction facility, able to display images and light curves in real time, even when running at the highest frame and data rates. Post observing, the pipeline acts as a multiplatform, feature-rich photometric reduction package, including optimal extraction (Naylor 1998). For quick-look reduction, most of the pipeline parameters are kept hidden and the observer can easily skip over the few that remain to view images and light curves as quickly as possible. Conversely, when reducing data for publication, the signal-to-noise ratio can be maximized by carefully tweaking every parameter. The pipeline

[4]https://hcam-finder.readthedocs.io/en/latest.
[5]http://deneb.astro.warwick.ac.uk/phsaap/hipercam/docs/html.

also offers an API (Application Programmers Interface), giving users access to raw HiPERCAM data using their own PYTHON scripts.

To ensure efficient writing speed and storage, the raw data and headers from a run on a target with HiPERCAM are stored in a single, custom-format binary FITS cube. Each slice of the cube contains five images, one from each of the HiPERCAM CCDs, and a timestamp. The file may contain millions of such slices if a high-speed observation is performed. The pipeline grabs these individual slices, or frames, for processing, and can write out standard-format FITS files containing a single exposure from the five HiPERCAM CCDs, if required.

Although autoguiding is provided at the GTC Folded Cassegrain focus used by HiPERCAM, secondary guiding from the science images is useful in cases where no guide stars can be found or to eliminate the effects of flexure between HiPERCAM and the guide-probe arm. Using stellar centroids calculated as part of the real-time data reduction, the pipeline is able to send regular right ascension and declination offsets to the TCS server to correct for any tracking errors.

3.4 Readout modes

HiPERCAM can be read out in three different modes: full-frame, windowed and drift mode, as shown in Fig. 4. In full-frame mode, the entire image area is read out, with an option to include the over-scan and pre-scan regions for bias-level determination. The windowed mode offers either one window in each quadrant (or one 'quad') or two windows in each quadrant (two quads), with an option to include the pre-scan (but not over-scan) regions. Drift mode is for the highest frame-rate applications, and uses just two windows lying at the border between the lower image and storage areas, as shown in Fig. 4 and described in greater detail below.

To ensure that the five HiPERCAM CCDs are read out simultaneously, and to simplify the data acquisition system, each window in a quad must have the same pixel positions in all five detectors. In addition, the data acquisition system expects data from each of the four outputs of the CCDs to be processed at the same time, which effectively means that the windows in a quad must lie the same number of pixels from the vertical centre-line of the detector. This restriction would make target acquisition difficult, so in practice a *differential shift* is performed during readout: The three windows in a quad lying furthest from their respective CCD outputs are shifted along the serial register to lie at the same distance from the output as the closest (fourth) window of the quad. A detailed description of the differential shift technique is given in appendix A2 of Dhillon et al. (2007).

The only restrictions on the sizes and positions of the windows are that they must not overlap with each other or with the borders between the readout quadrants, and that the windows in each quad must have identical sizes and vertical start positions. All windows must also have the same binning factors; pixels can be binned by factors of 1–12 in each dimension. These restrictions simplify the data acquisition system but still give flexibility in acquiring targets and comparison stars in the windows by adjusting the horizontal/vertical positions and sizes of the windows, the telescope position, and the instrument rotator angle. The HiPERCAM acquisition tool (see Section 3.2.2) can be used to assist in this process.

The CCDs in HiPERCAM are split frame-transfer devices, as shown in Fig. 4. When an exposure is finished, each image area is shifted into its corresponding storage area, and the next exposure begins. This frame-transfer process is quick – 7.8 ms with slow clocking (the corresponding figure for the fast clock setting is
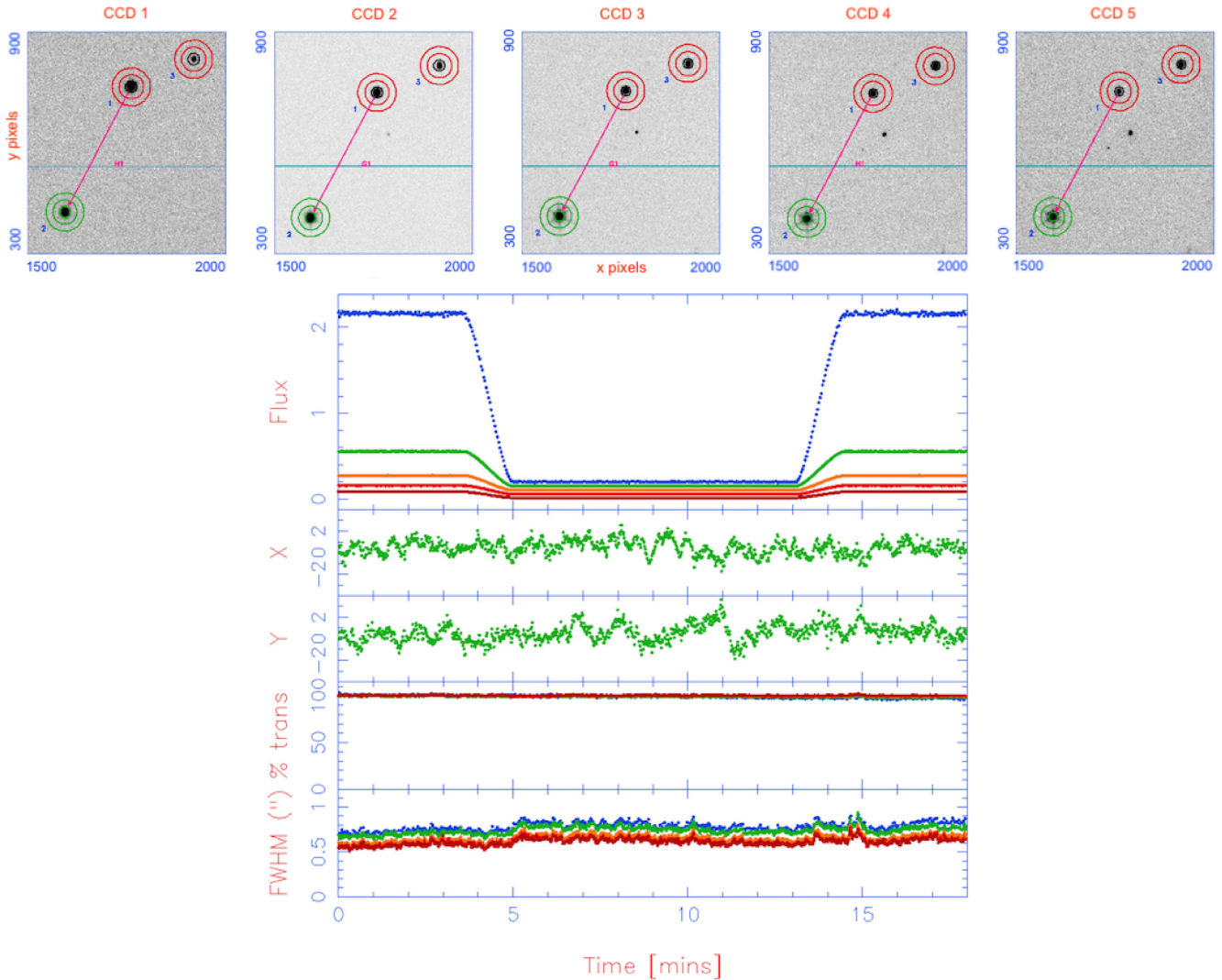
Figure 9. A screenshot of the HiPERCAM data-reduction pipeline. Top panel: zoomed-in images in $u_s g_s r_s i_s z_s$ of the target (the eclipsing red-dwarf/white-dwarf binary NN Ser) and two comparison stars, surrounded by software apertures defining the object and sky regions. Aperture 1 is the target, and apertures 2 and 3 are the comparison stars. Aperture 2 is green because it has been defined as the reference star for centroiding. The pink arrows show that the target and reference apertures are linked, so that the positional offset between the two is held constant when the target almost disappears during eclipse. Bottom panel: From the top to bottom, the target flux divided by the comparison star flux in $u_s g_s r_s i_s z_s$ (each with a flux offset of 0.05 added to separate the light curves during eclipse minimum), the comparison star x and y positions, the sky transparency measured from the comparison star flux, and the seeing measured from the comparison-star FWHM in $u_s g_s r_s i_s z_s$.

6.7 ms). During an exposure, the previous image in the storage area is vertically shifted into the serial register row-by-row, with any unwanted rows between the windows being dumped. Each row is then horizontally clocked along the serial register to the output where it is digitized,[6] with any unwanted pixels in the serial register lying either side of the windows being dumped. Therefore, whilst the current frame is exposing, the previous frame is being read out. The dead time between exposures is thus only 7.8 ms in HiPERCAM – the time it takes to shift the image into the storage area. The rapid shifting from image to storage area acts like an electronic shutter, and is much faster than a conventional mechanical shutter. The lack of mechanical shutters in HiPERCAM does result in vertical trails in

short-exposure images of bright stars, but these can be overcome in some situations using the focal-plane mask (see Section 3).

As well as two different clocking speeds (slow/fast), HiPERCAM also offers two pixel rates (slow/fast), as indicated in Fig. 4. Using the slow clock and pixel speeds, a full frame can be read out every 2.9 s with a dead time of 7.8 ms; the corresponding figures for the fast clock and pixel speeds are 1.1 s and 6.7 ms, respectively.

It is more complicated to set a precise exposure time with HiPERCAM than it is with a non-frame-transfer CCD. This is because it is not possible to shift the image area into the storage area until there is sufficient room in the storage area to do so. The fastest exposure time is therefore given by the time it takes to clear enough space in the storage area, which in turn depends on the window sizes, locations and binning factors, as well as the clocking and pixel rates, all of which are variables in the HiPERCAM data acquisition system. If an exposure time longer than the time it takes

---

[6]The word *digitization* here refers to both the determination of the pixel charge content via ACS and the digitization of the signal by the ADC. The frequency at which this occurs is referred to as the *pixel rate*.

to read out the storage area is required, an *exposure delay* must be added prior to the frame transfer to allow photons to accumulate in the image area for the required amount of time. On the other hand, if a shorter exposure than the time it takes to read out the storage area is required, the exposure delay must be set to zero and the binning, window and clocking/pixel rates adjusted so that the detector can frame at the required rate. Since the frame transfer time, i.e. the time required to vertically clock the whole image area into the storage area, is 7.8 ms in HiPERCAM, the maximum frame rate is limited to ∼122 Hz, but with a duty cycle (the exposure time divided by the sum of the exposure and dead times) of less than 5 per cent. With a more useful duty cycle of 75 per cent, the maximum frame rate is only ∼30 Hz.

For frame rates significantly faster than ∼30 Hz, a different readout method is required, known as *drift mode*. We originally developed this mode for ULTRACAM and ULTRASPEC (see Dhillon et al. 2007, 2014), and the readout sequence is shown pictorially and described in detail in fig. A1 and appendix A of Dhillon et al. (2007). Two windows, one for the science target and the other for a comparison star, are positioned at the bottom of the image area, next to the border with the storage area (see Fig. 4). At the end of an exposure, only the two windows, not the entire image area, are vertically clocked into the (top of) the storage area. The results in a stack of windows being present in the storage area at any one time, and a dramatic reduction in the dead time between exposures because it is now limited by the time it takes to move a small window rather than the full frame into the storage area. For example, two 4×4 binned HiPERCAM windows of size 32×32 pixels would take only 0.4 ms to move into the storage area in drift mode, providing a frame rate of ∼600 Hz with a duty cycle of 75 per cent – a factor of 20 improvement over windowed mode.[7]

Due to its complexity, drift mode only allows two windows to be used, with no pre-scan or over-scan regions and no clearing between frames. The only difference in how drift mode has been implemented in HiPERCAM compared to ULTRACAM is that two additional windows are read out by the upper two outputs of the HiPERCAM CCDs during drift mode, but the top half of the image area is obscured by the focal-plane mask and hence these windows are not processed by the data reduction pipeline.

Although drift mode has a clear advantage in terms of frame rate, it has the disadvantage that only two windows, instead of up to eight, are available. Also, drift mode windows spend more time on the CCDs, and hence accumulate more sky photons and more dark current. Hence, although the additional sky photons can be blocked by the focal-plane mask, and the dark current in HiPERCAM is negligible, it is recommended that drift mode should only be used when the duty cycle in non-drift mode becomes unacceptable, which typically occurs when frame rates in excess of about 30 Hz are required.

When observing bright standard stars or flat fields, it is sometimes necessary to take full-frame images with short exposure times. HiPERCAM therefore offers users the option of taking exposures of arbitrarily short length by turning CCD clearing on. When clearing is on, data in the image area are dumped prior to exposing for the required length of time. Hence any photoelectrons collected in the image area whilst the previous exposure is reading out are discarded. Clear mode has the disadvantage that the duty cycle is poor (25 per cent in the case of a full-frame 1-s exposure with the slow clocking and pixel speeds).

---

[7] A HiPERCAM frame-rate calculator can be found at: http://www.vikdhillon.staff.shef.ac.uk/hipercam/speed.html.

By default, all HiPERCAM CCDs start and end their exposures at exactly the same time. This synchronicity is of great scientific value when comparing the variability of sources at different wavelengths, but can result in significant signal-to-noise ratio variations between the bands if an object is particularly blue or red. It is possible for each of the HiPERCAM CCDs to have a different exposure time, and still ensure strict simultaneity of readout, by skipping the readout of selected CCDs using the *NSKIP* parameter in full-frame and windowed mode. For example, setting the exposure time to 2 s and NSKIP to 3,2,1,2,3 for the u_s, g_s, r_s, i_s, z_s CCDs would result in the NGC reading out only the r_s-band CCD on the first readout cycle (giving a 2-s r_s exposure), then the g_s-, r_s-, and i_s-band CCDs on the second readout cycle (giving a 4-s g_s and i_s exposure and a 2-s r_s exposure), and then the u_s-, r_s-, and z_s-band CCDs on the third readout cycle (giving a 6-s u_s and z_s exposure and a 2-s r_s exposure), etc.

The u_s-, r_s-, and i_s-band images experience an odd number of dichroic reflections, as shown in Fig. 1(b), and must therefore be corrected for the left-right flip compared to the g_s and z_s-band images. This is achieved by swapping the serial clocking between the E and H outputs, and the F and G outputs, in the u_s, r_s, and i_s CCDs (see Fig. 4). It is possible to swap the outputs in this way on individual CCDs because the sequencer scripts (see Fig. 8) for each CCD run on separate FEBs (see Fig. 7). An alternative option would have been to perform this output swapping by altering the cables between the $u_s r_s i_s$ CCDs and the NGC, but it is preferable from a cable design, manufacture, and maintenance perspective to have identical cables for all CCDs. Note that swapping the serial clocking is only necessary in windowed and drift modes – it is not required for full-frame readout as the image flip can be corrected in the data reduction pipeline.

4 PERFORMANCE ON THE GTC

HiPERCAM saw first light on the GTC in 2018 February, and it has since been in use for 13 observing runs totalling ∼70 nights (although some of these nights were shared with other instruments or partly lost due to weather). The first tranche of scientific papers based on HiPERCAM data have now been published (Nieder et al. 2019; Paice et al. 2019; Rebassa-Mansergas et al. 2019; Burdge et al. 2020; Kupfer et al. 2020a,b; Parsons et al. 2020; Montes et al. 2021; Paice et al. 2021; van Roestel et al. 2021). In this section, we summarize the performance of HiPERCAM on the GTC.

4.1 Image quality

We measured the plate scale of each CCD by stepping a bright star across the field of view by a known angle and measuring the movement in pixels. We find the same value of the plate scale in all five bands to within the errors, 0.0805 ± 0.0001 arcsec pixel^{-1}, as required (see Section 2.1.1).

In order to assess the image quality, we observed a dense stellar field during excellent seeing conditions, after aligning and focusing the secondary and segmented primary mirrors. The FWHM of stars at the centre of the images in each filter were measured to be 0.56/0.44/0.41/0.37/0.36 (±0.02) arcsec in $u_s g_s r_s i_s z_s$, respectively, with no significant deviations from these values in the corners of the field of view, as required (see Section 2.1.1). HiPERCAM on the GTC can therefore provide images that are seeing-limited across the whole field of view in even the best observing conditions on La Palma.

We do not expect to see any ghosting in HiPERCAM images (see Section 2.1) because the dichroics operate in a collimated beam and have antireflection coatings on their rear surfaces (see Section 2.1). This is indeed the case – the brightest (saturated) stars in the images
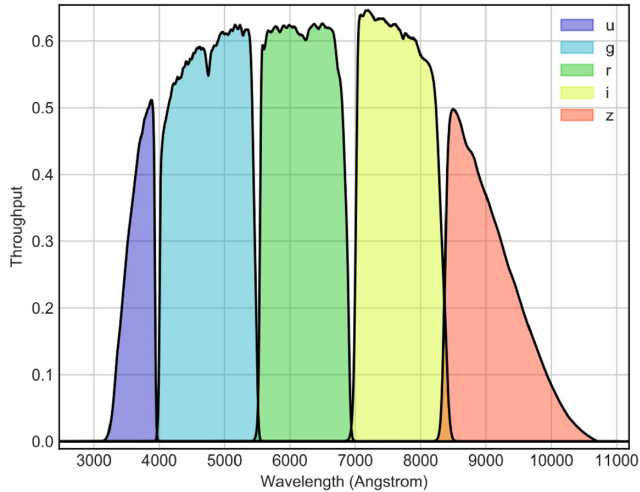
Figure 10. HiPERCAM throughput in the $u_s g_s r_s i_s z_s$ bands, not including the telescope and atmosphere.

Figure 11. Limiting magnitudes (5σ) of HiPERCAM on the GTC as a function of exposure time in $u_s g_s r_s i_s z_s$ (purple, blue, green, orange and red curves, respectively), assuming seeing of 0.6 arcsec, dark moon, and observing at the zenith.

show no discernible ghosting, down to a level given by the read noise, i.e. less than one part in 10^4. The pixel positions of the stars are the same to within approximately 5 pixels (75 μm) on all five CCDs, showing that the relative alignment of the CCD heads is good. We measured the vignetting from images of blank regions of the twilight sky, finding the field of view to be flat from the centre to the corners to better than ∼5 per cent.

4.2 Throughput and sensitivity

The HiPERCAM zero-points on the GTC, defined as the magnitude of a star above the atmosphere that gives 1 photo-electron per second in each filter, were measured from SDSS standard star observations (Smith et al. 2002) on photometric, non-dusty nights. We found values of 28.15/29.22/28.78/28.43/27.94 in $u_s g_s r_s i_s z$, respectively. The errors on these zero-points are estimated to be ±0.05 and are dominated by the uncertainty in the primary extinction coefficients, which we measured from the light curves of comparison stars observed on the same nights as the standards; we found typical atmospheric extinction values of 0.48/0.17/0.10/0.05/0.05 in $u_s g_s r_s i_s z$, respectively, consistent with the long-term values measured at the Observatorio del Roque de los Muchachos.[8] For comparison, OSIRIS (Cepa et al. 2003), the workhorse single-beam, red-optimized imaging spectrograph on the GTC, has observed zero-points of 25.76/28.26/28.84/28.49/27.95 in *ugriz*, respectively, demonstrating that HiPERCAM is competitive with OSIRIS in the red and superior in the blue.

We have estimated the response of the HiPERCAM optics and detectors by building a throughput model based on the measured lens/window/filter transmissions, dichroic reflectivities/transmissions, and the CCD QEs.[9] The throughput is shown as a function of wavelength in Fig. 10. It can be seen that the throughput peaks at over 60 per cent in $g_s r_s i_s$, exceeds 50 per cent in u_s and z_s, and there is some sensitivity even up to 1060 nm. This is more efficient than many single-beam imagers, e.g. the throughput of Keck/LRIS
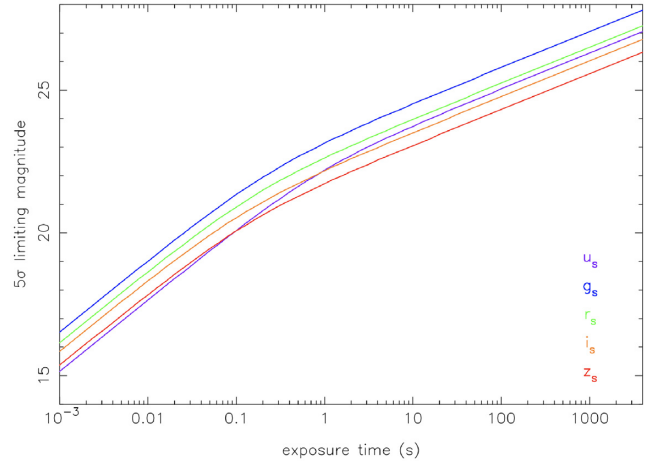
is 26/51/48 per cent in *BVR*,[10] respectively, despite the fact that HiPERCAM also has dichroic beamsplitters in the light path. The high throughput of HiPERCAM has been achieved by using CCDs and high-performance, multilayer coatings on the dichroics, filters, lenses, and windows that have each been optimized for operation in their bandpass, rather than for all bandpasses. Using the throughput model, we calculate theoretical HiPERCAM zero-points on the GTC of 28.09/29.22/28.86/28.52/27.92 in $u_s g_s r_s i_s z$, respectively, which agree to within a few per cent with the observed zero-points, demonstrating that the instrument is performing to specification. A detailed analysis of the HiPERCAM colour terms when using the Super SDSS filters is deferred to another paper (Brown et al., in preparation).

Fig. 11 shows the limiting magnitudes of HiPERCAM on the GTC as a function of exposure time, calculated from the measured zero-points. It is possible to obtain 5σ limiting magnitudes of $g_s \sim 23$ in 1 s and $g_s \sim 28$ in 1 h.[11]

4.3 Read noise and cross talk

The read noise of HiPERCAM is limited by the bandwidth of the pre-amplifier, which is currently hard-wired to 1.06 MHz (Bezawada et al. 2018) – see Section 5.3 for a future enhancement that will overcome this restriction. As a result, HiPERCAM currently has a read noise of ∼5.5 e⁻ at the fast pixel rate of 526 kHz, and ∼4.5 e⁻ at the slow pixel rate of 192 kHz (which involves averaging four samples of the charge content of each pixel in the NGC, each taken at ∼1 MHz). These read noise values were measured at the GTC using the dummy outputs of the CCDs to eliminate pickup noise, which theoretically increases the read noise by approximately a factor of $\sqrt{2}$ compared to so-called *single-ended mode*. However, we see significant pick-up noise at the telescope in single-ended mode and hence always use the dummy outputs whilst observing.

We also checked for cross-talk, due to the multiple outputs on the CCDs and their associated electronics. When a bright source is present in one of the CCD quadrants, cross-talk manifests itself as

---

[8]https://research.ast.cam.ac.uk/cmt/camc_extinction.html.

[9]The model uses the PYTHON module *pysynphot* and is available from https://github.com/StuartLittlefair/ucam_thruput.

[10]https://www2.keck.hawaii.edu/inst/lris/photometric_zero_points.html.

[11]A signal-to-noise ratio calculator for HiPERCAM + GTC is available at: http://www.vikdhillon.staff.shef.ac.uk/hipercam/etc.html.

a ghost image (positive or negative) at a mirrored position in the other quadrants (Freyhammer et al. 2001). We searched the mirror positions to bright (saturated) sources in HiPERCAM images and found no evidence for any cross-talk signal, down to a level given by the read noise, i.e. less than one part in 10^4.

4.4 Timestamping

Given that HiPERCAM can image at rates exceeding 1 kHz, it is important that each frame is timestamped to a significantly better accuracy than this, i.e. to better than ∼100 μs. To measure the timestamping accuracy, we observed an LED mounted on the focal-plane mask with HiPERCAM. The LED was triggered by the pulse-per-second (PPS) output of the GPS card to turn on precisely at the start of each UTC second, and off again half a second later. The accuracy of the PPS output is better than 50 ns and the LED rise time is of a similar order, so these are insignificant sources of error. The LED formed a pseudo-star in the images, which were reduced by the HiPERCAM data-reduction pipeline. The resulting light curves were then phase-folded on the 1-s period of the LED. The light curve shape is a convolution of two top-hat functions, one for the exposure time duration and the other for the LED pulse, resulting in the folded light curve showing a ramp. In the absence of any timestamping errors, the centre of the ramp should correspond to the start of the UTC second. We tested every readout mode in this way[12] and found that the LED turned on within ∼100 μs of the start of each UTC second, thereby meeting the absolute timestamping accuracy requirement of HiPERCAM. This test is insensitive to timestamping errors equal to an integer number of seconds, but it is difficult to see how such an error could arise in the HiPERCAM data acquisition system, and we would have noticed such a large error in our multi-instrument monitoring of eclipsing white dwarfs (e.g. Marsh et al. 2014).

We also measured the frame-to-frame stability of the HiPERCAM exposure times by measuring the time intervals between 5 million consecutive HiPERCAM drift-mode observations taken with a frame rate of 1 kHz: the exposure times remained constant to better than 100 ns.

4.5 Flexure

Whilst observing a star field, we turned the rotator through 180° and determined the location of the rotator centre, which we found lay (4, 12) pixels from the r_s-band CCD centre, verifying that the mechanical alignment of HiPERCAM is excellent. This measurement was made near the zenith and was then repeated at an altitude of approximately 40°. We found that the rotator centre values on all five CCDs were consistent between the zenith and 40° to within one pixel, indicating mechanical flexure of less than 15 μm at the detector, as required (see Section 3).

4.6 Reliability

HiPERCAM currently has only one moving part – the focal-plane slide, and hence it is an intrinsically reliable instrument. We estimate that we have lost less than 5 per cent of observing time due to technical problems with the instrument during the ∼70 nights that HiPERCAM has been in use on the GTC to date. The majority of this time loss has been due to problems with the flow sensors and the CCD vacuum seals. The flow-sensor problem has now been rectified by switching from the original Hall-effect flow sensors (which failed due to metallic particles in the coolant clogging up the magnetic rotors), to ultrasonic flow sensors (which also failed due to the presence of micro-bubbles in the coolant), to optical flow sensors (which appear to work well). The problems with the loss of vacuum in some of the CCD heads were mostly due to the copper gaskets used for the main case seals and have since been rectified by resealing.

5 FUTURE PLANS

With HiPERCAM now working to specification and entering its science exploitation phase at the GTC, we have begun a program of instrument enhancements to further improve its performance.

5.1 COMPO

To correct for transparency variations in the Earth's atmosphere, astronomers use the technique of differential photometry, where the target flux is divided by the flux of one or more comparison stars observed at the same time, and in the same patch of sky, as the target. In order not to degrade the signal-to-noise ratio of the resulting light curve significantly, it is necessary to use comparison stars that are brighter than the target star. If the target star is particularly bright, it becomes difficult to find suitable comparison stars, especially if the field of view of the photometer is small.

The probability of finding a comparison star of a given magnitude depends on the galactic latitude of the target and the search radius, and can be calculated from the star counts provided by Simons (1995). If the search radius is equal to the 3.1-arcmin (diagonal) field of view of HiPERCAM, the probability of finding a comparison star of magnitude $r_s = 14$ is 90 per cent at a Galactic latitude of 30° (the all-sky average).[13] Such a comparison star would be fainter than the brightest scientific targets observed with HiPERCAM, such as the host stars of transiting exoplanets, thereby limiting the signal-to-noise ratio of the differential light curve. In addition, most comparison stars are likely to be red, whereas the majority of HiPERCAM targets are blue, exacerbating the problem in the u_s-band in particular.

One way to increase the brightness of comparison stars available for differential photometry is simply to increase the field of view of the instrument. In the case of HiPERCAM, this can be achieved by replacing the existing collimator with a larger one, as described in Section 2.1. However, this would be extremely expensive and would only increase the diagonal field of view to 4.3 arcmin, giving a 90 per cent probability of finding a comparison star of magnitude $r_s = 13$, i.e. gaining only one magnitude in brightness. A much more effective and cheaper solution is to use the COMParison star Pick-Off system (COMPO) shown in Fig. 12. Light from a bright comparison star that falls within the 10.3 arcmin diameter field of view of the GTC Folded Cassegrain, focus but outside the 3.1-arcmin field of view of HiPERCAM, is collected by a pick-off arm lying just above the telescope focal plane. The light is then redirected to a second arm lying just below the focal plane, via some relay optics, which injects the starlight on to one of the bottom corners of the HiPERCAM CCDs. The effective field of view for comparison stars is hence increased to 6.7 arcmin, giving a 90 per cent probability of finding a comparison star of magnitude $r_s = 12$, i.e. gaining two magnitudes in brightness.

---

[12]For details, see http://deneb.astro.warwick.ac.uk/phsaap/hipercam/docs/html/timing/timing_tests.html.

[13]A comparison star probability calculator is available at http://www.vikdhillon.staff.shef.ac.uk/ultracam/compstars.html.
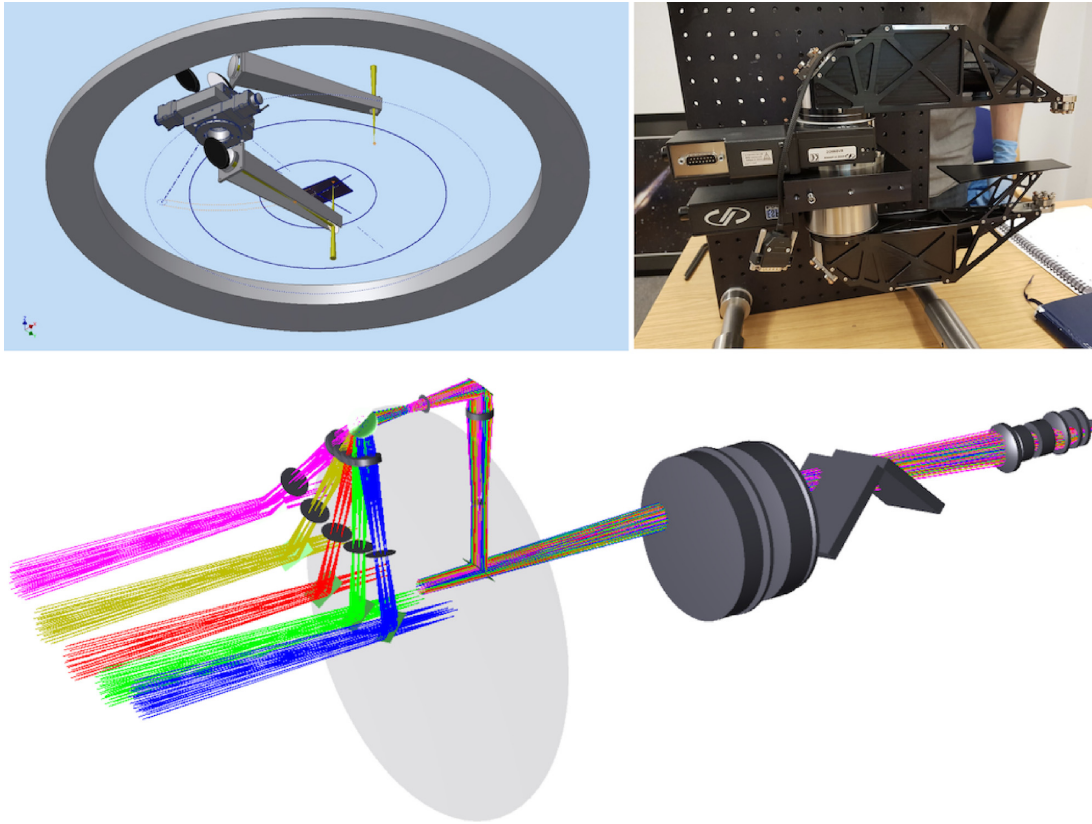
Figure 12. Top left-hand panel: schematic of COMPO, looking up at the telescope focal plane. The HiPERCAM field of view is indicated by the filled blue rectangle at the centre. The upper (pick-off) arm collects light from a star, indicated by the upper yellow cone of light, falling outside the HiPERCAM field of view but inside the 10.3-arcmin diameter view of view at the GTC Folded Cassegrain focus (outer solid blue circle). The lower (injection) arm redirects this light via some relay optics to one of the corners of the HiPERCAM field of view, indicated by the lower yellow cone of light. Top right-hand panel: photograph of COMPO during assembly in the lab, showing the pick-off arm (top panels) and injection arm (bottom panels) attached to their respective rotation stages. The baffle attached to the injection arm can be seen at the right. Bottom panels: ray trace through the COMPO optics. Light from the GTC at the left is incident on the pick-off mirror, shown at five different off-axis angles by the coloured beams. The light first passes through a field stop and collimator lens in the pick-off arm, which are mounted on a motorized linear stage to compensate the focus for the curved telescope focal plane (shown by the large, light-grey ellipse). The light is then redirected to the injection arm via two fold mirrors, and passes through a re-imaging lens and another field stop before being reflected by the injection mirror into HiPERCAM (displayed on the right with dark grey lenses/dichroics – only the z_s arm is shown).

The pick-off and injection arms rotate around a fixed point that lies outside the patrol field, as shown in Fig. 12. The rotation axis of the arms is tilted to align it with the telescope exit pupil. The internal relay optics of the pick-off arm include a collimator and field stop to eliminate off-axis rays and help control stray light, which are together mounted on a motorized linear stage that moves along the optical axis to compensate for the curvature of the telescope focal plane.

Attenuation of the comparison-star light within COMPO is unimportant, as long as it remains constant during the observation. The pick-off has a square field of view of side 24 arcsec and this is injected on to a square of side 330 pixels in the corner of each CCD. A baffle mounted at the end of the injection arm and positioned close to the telescope focal plane is used to prevent any light scattered by the COMPO arms from entering the instrument and also gives a sharp edge to the injected field in the final image. The rest of the field of view of HiPERCAM is unaffected by COMPO, so any other comparison stars that fall in the image can be used as before. Users will be able to select suitable comparison stars for COMPO using the acquisition tool described in Section 3.2.2. For users who do not need to use COMPO, the arms can be fully retracted out of the beam.

The manufacture of COMPO is now complete and we hope to commission the system at the GTC during 2022.

5.2 Diffuser

When observing the brightest sources with HiPERCAM, such as the host stars of transiting exoplanets, the signal-to-noise ratio in a differential light curve can be limited by variations in seeing or atmospheric scintillation, rather than the brightness of the target or comparison stars (see Osborn et al. 2015 and Föhring et al. 2019). In the case of seeing, the varying PSF alters the fraction of light falling outside the photometry software aperture in a way that differs between the target and comparison stars, due to the fact that the latter almost always lie outside the isoplanatic patch (only ∼2 arcsec in the optical on La Palma; Vernin & Muñoz-Tuñón 1994) of the former. Simply increasing the size of the software aperture is not a solution due to the corresponding increase in sky and read noise, and profile fitting is unable to model the subtle changes in PSF due to rapid seeing variations. It is possible to create a more stable PSF by defocusing the telescope (e.g. Southworth et al. 2009), but the

most stable PSFs are only achievable using beam-shaping diffusers (Stefánsson et al. 2017).

We have tested such a diffuser in HiPERCAM on the GTC. The diffuser was placed in front of the collimator and, as expected, gave a much more stable PSF compared to using telescope defocusing. The diffuser we tested was not optimized for HiPERCAM – the diameter of the diffuser was only 150 mm, rather than the required 225 mm, and hence there was vignetting at the edge of the HiPERCAM field of view. In addition, the throughput of the diffuser fell from >90 per cent in $g_s r_s i_s z_s$ to ~70 per cent in u_s, due to the non-optimized diffuser polymer, substrate and AR coatings used. Therefore, it is our intention to procure a new, custom diffuser for HiPERCAM that has a larger diameter and higher u_s-band throughput. By combining this new diffuser with COMPO, HiPERCAM on the GTC will become the perfect tool for ground-based, broad-band transmission-photometry studies of the atmospheres of transiting exoplanets.

5.3 Read noise

We aim to reduce the read noise of HiPERCAM to approximately $3 e^-$ using a combination of measures, including: introducing a software-switchable bandwidth in the pre-amplifier so that reduced bandwidths in combination with slower pixel rates can be used to reach the read-noise floor of the system; reducing the bandwidth in the NGC FEBs from the current value of 3.9 MHz to approximately 2 MHz; reducing the voltage noise of the op-amps and the resistance of the resistors (to reduce their thermal noise) in the pre-amplifier; replacing the bias and clock cables running between the pre-amplifier and NGC with twisted pairs and braided shields. All of these modifications are now under test in the lab, and the most effective ones will be implemented in HiPERCAM during 2022.

5.4 New rotator

HiPERCAM is currently mounted on the Folded Cassegrain E focus of the GTC, which it currently shares with at least two other instruments.[14] This means that HiPERCAM has to be mounted/dismounted from the telescope once or twice a year, restricting the amount of available telescope time and the fraction of sky that can be accessed, and results in HiPERCAM sometimes being unavailable for following-up exciting new astronomical events. Sharing the focus with other instruments also means that every HiPERCAM run involves a significant amount of extra staff time to mount/dismount the instrument at the start/end, and risks damage to the instrument each time it is moved.

We have identified a solution to this problem – the GTC has a third Folded Cassegrain focus, labelled G, that has never been used. This focus is currently just a hole in the steel structure of the telescope through which the telescope beam can be steered by the tertiary mirror. The focus currently has no image derotator (commonly referred to as a *rotator*), cable wrap, autoguider, or services (electricity, ethernet, coolant). The reason this focus has never been commissioned by the GTC is that the surrounding space envelope is too small to fit their common-user instrumentation. But this is not a problem for HiPERCAM, which as a visitor instrument was designed to be as compact as possible, and is far smaller than any of the other GTC instruments.

We have recently completed a preliminary design study of a compact rotator for HiPERCAM that can fit in the available space

envelope. One way in which space has been saved is by not incorporating a traditional autoguider mechanism with a probe arm mounted on an azimuthal track in the rotator. Instead, autoguiding with the new rotator will be provided in two ways. For high-speed observations (seconds and below), guiding will be performed from the HiPERCAM science images, as described in Section 3.3. For deep imaging, for which COMPO becomes redundant, we shall use COMPO for autoguiding, with the pick-off arm selecting guide stars outside the HiPERCAM field of view and the injection arm redirecting the light to a separate autoguider camera fixed to the interface collar on which COMPO is mounted (see Fig. 3).

We plan to begin manufacture of the new rotator in 2021, with commissioning on the telescope during 2022.

6 CONCLUSIONS

We have presented the design of HiPERCAM and demonstrated that it is performing to specification on the GTC. We have also described some of the future upgrades planned for the instrument, including a novel comparison-star pick-off system. HiPERCAM provides the GTC with a unique capability amongst the world's 8–10 m class telescopes and is a powerful new tool in the field of time-domain astrophysics.

DATA AVAILABILITY

Only commissioning data are reported on in this paper. The data will be shared on reasonable request to the corresponding author.

REFERENCES

Antoniadis J. et al., 2013, Science, 340, 448
Baade D. et al., 2009, The Messenger, 136, 20

[14]http://www.gtc.iac.es/instruments/instrumentation.php.

Bezawada N. et al., 2018, in Holland A. D., Beletic J., eds, Proc. SPIE Conf. Ser. Vol. 10709, High Energy, Optical, and Infrared Detectors for Astronomy VIII. SPIE, Bellingham, p. 1070924

Burdge K. B. et al., 2020, ApJ, 905, 32

Cepa J. et al., 2003, in Iye M., Moorwood A. F. M., eds, Proc. SPIE Conf. Ser. Vol. 4841, Instrument Design and Performance for Optical/Infrared Ground-based Telescopes. SPIE, Bellingham, p. 1739

Dhillon V. S. et al., 2007, MNRAS, 378, 825

Dhillon V. S. et al., 2014, MNRAS, 444, 4009

Dhillon V. S. et al., 2016, in Evans C. J., Simard L., Takami H., eds, Proc. SPIE Conf. Ser. Vol. 9908, Ground-based and Airborne Instrumentation for Astronomy VI. SPIE, Bellingham, p. 99080Y

Dhillon V. S. et al., 2018, in Evans C. J., Simard L., Takami H., eds, Proc. SPIE Conf. Ser. Vol. 10702, Ground-based and Airborne Instrumentation for Astronomy VII. SPIE, Bellingham, p. 107020L

Dyer M. J., Dhillon V. S., Littlefair S., Steeghs D., Ulaczyk K., Chote P., Galloway D., Rol E., 2018, in Peck A. B., Seaman R. L., Benn C. R., eds, Proc. SPIE Conf. Ser. Vol. 10704, Observatory Operations: Strategies, Processes, and Systems VII. SPIE, Bellingham, p. 107040C

Föhring D., Wilson R. W., Osborn J., Dhillon V. S., 2019, MNRAS, 489, 5098

Freyhammer L. M., Andersen M. I., Arentoft T., Sterken C., Nørregaard P., 2001, Exp. Astron., 12, 147

Fukugita M., Ichikawa T., Gunn J. E., Doi M., Shimasaku K., Schneider D. P., 1996, AJ, 111, 1748

Gandhi P. et al., 2017, Nat. Astron., 1, 859

Graham M. J. et al., 2019, PASP, 131, 078001

Kirk J., Wheatley P. J., Louden T., Littlefair S. P., Copperwheat C. M., Armstrong D. J., Marsh T. R., Dhillon V. S., 2016, MNRAS, 463, 2922

Kupfer T. et al., 2020a, ApJ, 891, 45

Kupfer T. et al., 2020b, ApJ, 898, L25

Levin Y., Beloborodov A. M., Bransgrove A., 2020, ApJ, 895, L30

Littlefair S. P., Dhillon V. S., Marsh T. R., Gänsicke B. T., Southworth J., Watson C. A., 2006, Science, 314, 1578

LSST Science Collaboration, 2009, preprint (arXiv:0912.0201)

Lyman J. D. et al., 2018, Nat. Astron., 2, 751

Marsh T. R. et al., 2014, MNRAS, 437, 475

Marsh T. R. et al., 2016, Nature, 537, 374

Montes M., Trujillo I., Infante-Sainz R., Monelli M., Borlaff A. S., 2021, preprint (arXiv:2106.10283)

Naylor T., 1998, MNRAS, 296, 339

Nieder L. et al., 2019, ApJ, 883, 42

Ortiz J. L. et al., 2012, Nature, 491, 566

Osborn J., Föhring D., Dhillon V. S., Wilson R. W., 2015, MNRAS, 452, 1707

Paice J. A. et al., 2019, MNRAS, 490, L62

Paice J. A. et al., 2021, MNRAS, 505, 3452

Parsons S. G. et al., 2017, MNRAS, 470, 4473

Parsons S. G. et al., 2020, Nat. Astron., 4, 690

Raskin G., Morren J., Pessemier W., Perez Padilla J., Vandersteen J., 2013, preprint (arXiv:1311.0685)

Rebassa-Mansergas A., Parsons S. G., Dhillon V. S., Ren J., Littlefair S. P., Marsh T. R., Torres S., 2019, Nat. Astron., 3, 553

Simons D. A., 1995, Longitudinally Averaged R-Band Field Star Counts Across the Entire Sky. Gemini Observatory Technical Note No. 30, Hawaii and Chile

Smith J. A. et al., 2002, AJ, 123, 2121

Southworth J. et al., 2009, MNRAS, 396, 1023

Stefánsson G. et al., 2017, ApJ, 848, 9

Trujillo I., Fliri J., 2016, ApJ, 823, 123

Tulloch S., 1995, Investigation of Low Fringing Detectors on the ISIS Spectrograph. Isaac Newton Group, La Palma

van Roestel J. et al., 2021, preprint (arXiv:2107.07573)

Vernin J., Muñoz-Tuñón C., 1994, A&A, 284, 311

Wilson R. W., O'Mahony N., Packham C., Azzaro M., 1999, MNRAS, 309, 379

This paper has been typeset from a TEX/LATEX file prepared by the author.